Journal of Metals, Materials and Minerals, 36(2), e2461, 2026

Two-step sputtering for depositing smooth and thin ZnO films on non-heated, non-epiready PET substrates

Nattaya Tajina YOSSAPONG[1], Annop KLAMCHUEN[2], Kittipong TANTISANTISOM[2], Ekkaphop KETSOMBUN[3], Taworn INTARO[4], Sakuntam SANORPIM[1,5], and Warakorn YANWACHIRAKUL[1,5,*]

[1] *College of Interdisciplinary and Integrative Studies of Nanoscience and Technology, Chulalongkorn University, Phayathai, Bangkok, 10330, Thailand*
[2] *National Nanotechnology Center (NANOTEC), National Science and Technology Development Agency (NSTDA), Khlong Luang, Pathum Thani, 12120, Thailand*
[3] *Department of Physics, Faculty of Science, King Mongkut's University of Technology Thonburi (KMUTT), Thung Khru, Bangkok, 10140, Thailand*
[4] *Faculty of Science and Agricultural Technology, Rajamangala University of Technology Lanna (RMUTL), Phan, Chiang Rai, 57120, Thailand*
[5] *Department of Physics, Faculty of Science, Chulalongkorn University, Phayathai, Bangkok, 10330, Thailand*

***Corresponding author e-mail**: warakorn.y@chula.ac.th

Received date:
5 July 2025
Revised date:
14 July 2025
Accepted date:
21 July 2025

Keywords:
Oxide material;
Polyethylene terephthalate (PET);
Flexible substrate;
Sputtering;
Surface

Abstract

Highly crystalline, smooth-surface, and thin zinc oxide (ZnO) films have been successfully deposited on flexible polyethylene terephthalate (PET) substrates using an optimized two-step RF magnetron sputtering technique at ambient temperature. The PET used in this study was a commercially available overhead projector film, which was not epiready-grade and had a lower melting point (~150°C). This issue made high-quality deposition more challenging. In the first step, a thin ZnO buffer layer was deposited at low RF power to provide a smooth and thermally stable surface. This layer served as both a structural template and a thermal barrier during the subsequent high-power deposition of the main ZnO film. Structural analysis confirmed that the buffer layer suppressed lattice mismatch and reduced residual stress. The resulting film showed low surface roughness and no cracking. These features exceeded those of films grown directly at high power, which suffered from poor surface morphology due to substrate deformation. Although the use of a polycrystalline buffer layer led to a reduction in optical transmittance from increased light scattering, the fine-grained structure contributed to improved mechanical stability and dielectric loss suppression. These characteristics made films particularly suitable for piezoelectric applications on flexible substrates. This proposed two-step technique effectively balanced between surface smoothness and structural quality and offered practical solution for the fabrication of high-performance films on thermally sensitive substrates.

1. Introduction

Zinc oxide (ZnO) films deposited on polyethylene terephthalate (PET) substrates contribute to a wide range of applications in fields such as ultraviolet (UV) filtering coatings and other high-performance optoelectronic devices, for example, transparent insulating layers for touch screens and flat-panel displays [1,2]. Its robust luminescence facilitates advancements in UV and visible light-emitting diodes (LED) with minimized leakage current. This results in an improvement of sensitivity and a reduction in noise [3]. In terms of perspective, its piezoelectric characteristics enable the development of micro-scale energy harvesters and mechanical sensors [3,4]. The integration of ZnO films on PET substrates offers a promising platform for flexible piezoelectric devices such as pressure, bending, and vibration sensors [5-7]. ZnO itself has intrinsic piezoelectric properties, which permit it to generate electrical charges in response to mechanical stress and, conversely, to produce mechanical vibrations when applied by an electric field. This dual functionality is fundamental to the operation of piezoelectric micro-sensors that convert mechanical input into measurable electrical output [8]. Compact and high-resolution micrometer-scale devices can be easily fabricated into thin films or nanostructures using ZnO. Owing to its wide direct bandgap (3.37 eV) and large exciton binding energy (60 meV) at room temperature, this material provides strong excitonic stability [9]. Meanwhile, flexibility, low cost, and favorable mechanical strength and chemical resistance of PET make it a suitable substrate for wearable and conformal electronic devices [1]. This high-grade polyester also has high optical transmittance (~90% in the 400 nm to 800 nm visible range) [10]. When ZnO is deposited onto PET, the resulting structure combines mechanical adaptability with efficient signal conversion.

To achieve high-performance ZnO-on-PET piezoelectric devices, it is essential to control the material characteristics including smooth surface, low residual stress, strong c-axis crystal orientation, and fine crystallite size [11]. A smooth surface improves signal uniformity and ensures good contact with electrodes. Low residual stress preserves structural integrity and maintains piezoelectric function. A strong

c-axis crystal orientation enhances charge generation efficiency. Fine crystallite size increases mechanical stability and reduces dielectric loss. Previous study [12] has shown that films with smaller crystallite grains tended to exhibit more responsive domain wall motion under external mechanical or electrical excitation. This characteristic could improve sensor sensitivity and dynamic response in the films.

Although several fabrication techniques have been developed for ZnO films, including sol-gel processes, chemical vapor deposition (CVD), and pulsed laser deposition, these methods involve high-temperature processing steps or post-annealing that are incompatible with PET substrates to achieve high-quality films [13]. The relatively low melting point of PET (~200°C to 300°C) and its significant thermal expansion coefficient mismatch with ZnO (2.0×10^{-5} K^{-1} for PET versus 4.75×10^{-6} K^{-1} for ZnO) become challenges for the high-temperature film deposition [14,15]. In practical applications, PET substrates used in several studies were epiready-grade, with a melting point typically around 250°C, which offered improved thermal resistance during deposition. However, in this study, a commercially available, non-epiready PET film (commonly used for overhead projector transparency sheets) has been selected. This grade of PET has a much lower melting point of approximately 150°C. This feature makes it more susceptible to thermal deformation during sputtering, particularly at higher RF powers, thereby increasing the challenge of depositing smooth and highly crystalline ZnO films. High thermal stress resulting from the large mismatch between the thermal expansion coefficients of ZnO and PET led to substrate deformation, surface roughening, and film cracking during the deposition and cooling processes [2]. In addition, the residual stress induced under such conditions may reduce the adhesion between the film and the substrate. This phenomenon potentially caused delamination and film breakage. These limitations complicated the direct growth of high-quality ZnO films on PET at high temperatures. Among the available deposition approaches, radio-frequency (RF) magnetron sputtering has been proposed as a promising alternative technique for depositing ZnO at ambient temperatures. However, achieving high-quality and thin ZnO films on flexible PET substrates remained challenges [16].

Recent research has explored various approaches to enhance the growth quality of direct growth ZnO films on flexible PET substrates. Nevertheless, challenges remained diminishing stress-related defects, suppressing interfacial dislocations from lattice mismatch, inhibiting impurity diffusion from the substrate, and addressing rough surfaces and substrate deformation. For instance, Banjaree *et al.* [17] deposited ZnO films with thicknesses ranging from 260 nm to 470 nm using DC sputtering at low temperatures. However, the resulting films showed poor crystallinity, as indicated by weak and broadened X-ray diffraction (XRD) peaks. In contrast, Fernandez and Naranjo [13] used RF magnetron sputtering to deposit Al-doped ZnO (AZO) films with thicknesses between 500 nm and 700 nm. The films demonstrated improved (002) crystallographic orientation at reduced RF power levels. A related study by Ahmad *et al.* [18] investigated ZnO thin films deposited by RF magnetron sputtering at room temperature. Their results showed that increasing the RF power from 50 W to 250 W led to an increase in both film thickness and surface roughness. Similarly, Faraj and Ibrahim [19] used thermal evaporation to fabricate ZnO films with thicknesses from 100 nm to 300 nm and observed that surface roughness increased with film thickness. Furthermore, Demircioglu *et al.* [20] reported that high sputtering power in the range of 300 W to 500 W led to the deformation of the PET substrate, which in turn deteriorated the surface morphology of the ZnO films. These works mentioned the trade-off between deposition energy and surface morphology.

To solve these challenges, a two-step deposition technique incorporating a buffer layer has emerged as an effective method under ambient temperature conditions. The buffer layer behaved as the intermediary between the film and the substrate that alleviated stress-related defects, suppressed interfacial dislocations due to lattice mismatch, and limited impurity diffusion from the substrate. Furthermore, it induced the growth of well-aligned crystalline grains and enhanced both crystallinity and surface uniformity. This dual-function layer served as both a structural template and a thermal barrier that protected the substrate from heat-induced deformation during high-power deposition [21,22].

The success of this approach strongly depended on the careful selection and optimization of the buffer layer. Several materials have been widely used as buffer layers, such as GaN [23], Al_2O_3 [6,24], SiO_2 [25], CaF_2 [26], ZnS [27], and ZnO [21,28,29]. The advantage of homo-buffer layers lied in their ability to facilitate the homoepitaxy that created a perfect template [21]. This inherently minimized lattice mismatch and, consequently, avoided issues arising from a difference of thermal expansion coefficients between the buffer and the film, which was a common problem with the hetero-buffer layers [22].

The optimal condition, however, depended on several factors, including the intended application of the devices and the deposition methods. Additionally, accurate control of the thickness and structural properties of the buffer layer was a significant aspect. An excessively thin buffer might be insufficient to reduce thermal or interfacial stress, while an overly thick layer could introduce high electrical resistance [2,21]. Recently, the improvement of ZnO film properties with the buffer layer was reported. While the fabrication of ZnO on PET has being developed, the recent progress primarily involved layers thicker than 200 nm. For example, Gallium Zinc Oxide (GZO) and Al-doped ZnO (AZO) films with thicknesses in the range of 200 nm to 1600 nm were deposited using various buffer materials such as ZnO or other metallic interlayers [16,30–34]. In contrast, recent progress in the development of thin ZnO films on the order of 100 nm remains limited, due to ongoing challenges related to thermal sensitivity, stress management, and film uniformity on flexible PET substrates [6,24]. Solving these issues is particularly important for scenarios demanding thin active layers, where both mechanical compliance and high functional performance of the films are required for the respective applications.

In this work, we aimed to enhance the quality of ZnO films on non-epiready PET substrates for integration into piezoelectric micro-sensors and flexible electronic devices. To achieve this, an optimized two-step RF magnetron sputtering process has been investigated for depositing a 100 nm ZnO main film at an ambient temperature. The study had been allocated into two main parts. In the first part, the direct deposition of 100 nm ZnO films on PET under various power conditions was examined to identify suitable power settings for both the buffer and main layers. Based on these results, the optimal power conditions, low power for minimizing surface roughness in the buffer layer and high power for maximizing crystallinity in the main film,

were applied into the second part, focusing on the two-step deposition process. In this part, the thickness of the ZnO homo-buffer layer was further optimized to achieve high-quality films with balanced surface smoothness and crystallinity.

2. Experimental details

ZnO films were deposited onto PET substrates using RF magnetron sputtering (UNIVEX350 RF/DC, Oerlikon Leybold vacuum GmbH, Germany) without any intentional thermal treatment. The PET substrates used in this study were commercially available overhead projector transparent films with a thickness of approximately 140 μm and a surface area of 30 cm^2. Its low thermal resistance increased the feasibility of substrate deformation during high-power sputtering which made the deposition of high-quality, smooth ZnO films on such substrates more challenging.

Before deposition, each PET substrate was cleaned in an ultrasonic bath, first in ethanol (CAS No. 64-17-5, Merck) for 15 min, followed by isopropyl alcohol (IPA) (CAS No. 67-63-0, Merck) for another 15 min to remove any organic contaminants. After cleaning, nitrogen (N_2) with a 99% purity (CAS No. 7727-37-9, Praxair Co., Ltd.) was used to blow-dry the substrates to eliminate residual moisture.

Argon (Ar) with a 99.999% purity (CAS No. 7440-37-1, Praxair Co., Ltd.) was used as the sputtering gas and introduced into the chamber at a constant flow rate of 20 sccm. The background pressure before sputtering and the working pressure during deposition were maintained at 1.0×10^{-6} and 5.0×10^{-3} mbar, respectively. The ZnO target, with 99.95% purity, had a diameter of 3 inches and a thickness of 0.25 inches (Singapore Advantec PTEC Ltd.). Prior to each deposition, a 30 min pre-sputtering process was performed to clean the target surface and remove contaminants.

The samples were divided into two sets, as illustrated in Figure 1. The first set contained four samples, shown in Figure 1(a), where a 100 nm thick ZnO main film was directly deposited onto the PET substrate. RF power was varied across the samples at 50 W, 100 W, 150 W, and 200 W. Based on our experimental calibration, the corresponding sputtering rates were determined to be approximately 1.1 $nm \cdot min^{-1}$ at 50 W, 1.9 $nm \cdot min^{-1}$ at 100 W, 4.0 $nm \cdot min^{-1}$ at 150 W, and 4.6 $nm \cdot min^{-1}$ n at 200 W. These rates were used to precisely control the thickness of all direct-growth samples at 100 nm. The second set followed the two-step deposition process, shown in Figure 1(b). In this configuration, a ZnO buffer layer was first deposited onto the PET substrate at 50 W, and its thickness was controlled at 20 nm, 40 nm, 60 nm, and 90 nm using the 1.1 $nm \cdot min^{-1}$ rate obtained at this power. A 100-nm-thick ZnO main film was subsequently deposited on top of the buffer layer using a higher RF power of 150 W, at the rate of 4.0 $nm \cdot min^{-1}$. It was noted that the sputtering system used in this study did not include a temperature sensor for in-situ monitoring of surface temperature during deposition. Thus, the direct measurement of thermal effects on the substrate could not be performed.

Surface morphology and film thickness were analyzed using field emission scanning electron microscopy (FESEM, JSM-7001F) and atomic force microscopy (AFM, SEIKO SPA400). Three-dimensional (3D) surface visualizations were obtained from SEM images using ImageJ software. Structural and optical properties were evaluated under ambient conditions using a high-resolution X-ray diffractometer (HR-XRD, Bruker D8 Discovery) and UV-near IR spectrometer (Cary5000 UV-Vis-NIR), respectively.

3. Results and discussion

3.1 Direct deposition: 100 nm ZnO/PET

The direct deposition process significantly affected the morphological and structural characteristics of ZnO films on PET substrates. The experimental results showed two distinct regimes of film quality corresponding to low and high RF power. An overview of surface morphology, including the SEM and AFM images of 100 nm ZnO/PET shown in Figure 2, indicated that the films deposited at low power are smoother than those deposited at high power.

The SEM images shown in Figures 2(a-d) were visualized over an area of 24×18 μm^2. At 50 W, the film showed a relatively smooth surface with visible discontinuities and unmerged grain boundaries. These features were indicative of incomplete grain coalescence due to limited surface diffusion of adatoms on the substrate. Increasing the RF power to 100 W improved grain coalescence, leading to a more continuous film. At 150 W, enhanced adatom mobility further improved homogeneity of the film surface; however, elevated substrate temperatures at this power also induced thermal deformation, resulting in surface waviness. At 200 W, the morphological deformation became more severe, with distinct undulations and surface cracks. These cracks resulted from accumulated thermal stress and mechanical strain due to the mismatch in thermal expansion coefficients between the film and the substrate.

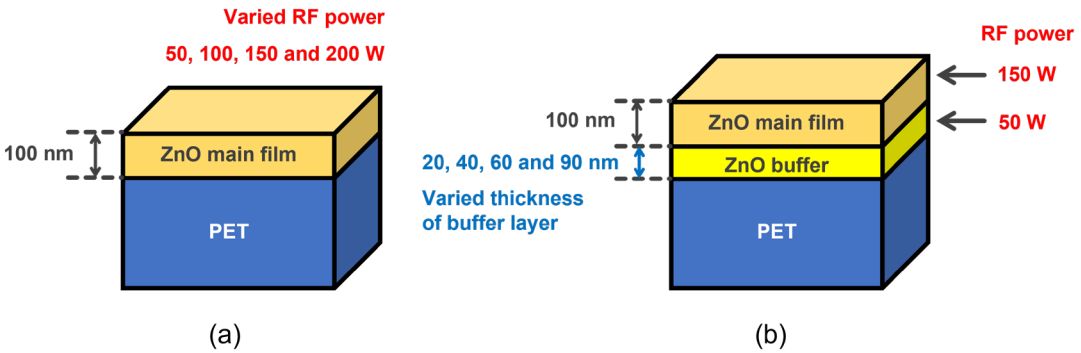

Figure 1. Details of the sample structures. (a) ZnO main film directly deposited on PET substrate, and (b) ZnO main film deposited with ZnO buffer layer on non-epiready PET substrate.

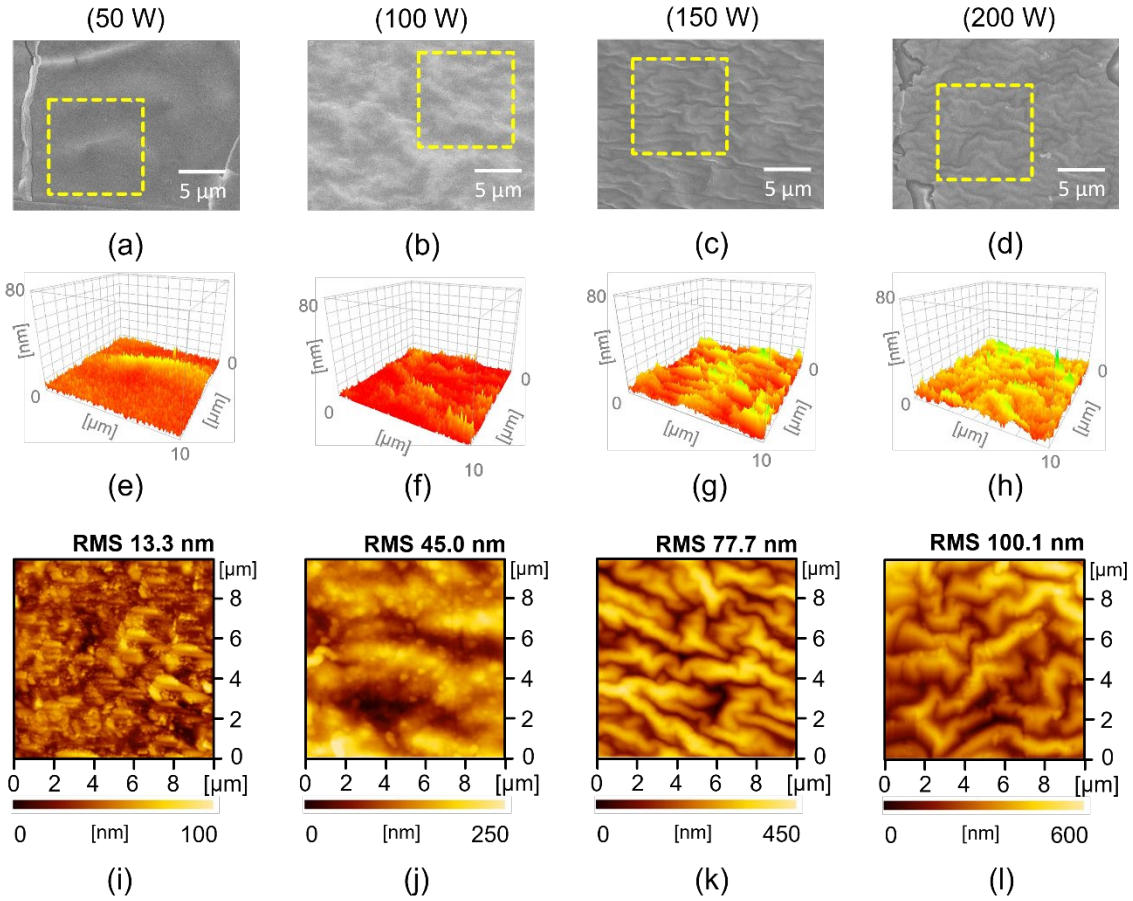

Figure 2. (a–d) SEM images, (e–h) 3D surface reconstructions from SEM data, and (i–l) AFM images showing the surface morphology of ZnO main films directly deposited on PET substrates. The RF power varied from 50 to 200 W.

This observed deformation at relatively low power (above 150 W) contrasted with the previous study [18] reporting that PET substrates could withstand sputtering at RF powers up to 250 W without deformation. One possibility was because of the difference in PET grades. In this study, a commercially available PET film was employed. This type of PET has a lower thermal tolerance, with a melting point of approximately 150°C, compared to the epiready-grade PET often used in previous research, which typically melts around 250°C. The lower thermal resistance of the PET in this work made it more susceptible to deformation under high-power deposition.

To further examine the surface topography, 3D images shown in Figures 2(e–h) had been generated using data acquired from the selected area of the original SEM images. At 50 W, the surface remained relatively flat, with only minor ridges attributed to grain boundary interactions. As power increases, surface undulations were more prominent. At 200 W, severe morphological irregularities dominated the surface profile. This result indicated that thermal expansion mismatch was a primary factor which contributed to the increased roughness and deformation.

AFM images in Figures 2(i–l) provided quantitative evaluation of the surface roughness in the 10 µm × 10 µm scan area. The root mean square (RMS) roughness increased markedly from 13.3 nm at 50 W to 100.1 nm at 200 W. Although the films at lower powers showed finer granular structures, the increase in grain size with higher power correlated with the loss of topographical uniformity. These AFM results were consistent with SEM observations and reinforced the role of thermal effects in influencing surface morphology.

Figure 3 illustrates the growth mechanisms and resulting effects of direct ZnO deposition on PET substrates under both low and high-power conditions, as summarized from the SEM and AFM analyses. At low power, the sputtered ions had insufficient energy for surface migration. As a result, the film formed a polycrystalline structure with relatively low surface roughness. At high power, the ions gained enough energy for surface migration. An increase of ion energy eliminated grain boundaries and induced the formation of homogeneous ZnO film. However, this increased energy input also raised the substrate surface temperature. Given the low melting point of the PET used in this study, the elevated temperature easily led to thermal deformation of the substrate, which dominantly caused an increase of surface roughness and morphological instability in the resulting film.

The interface between ZnO and PET had been investigated by cross-sectional SEM images shown in Figure 4. The schematic in Figure 4(a) illustrates the processes of sample preparation. The processes involved cleaving the sample, followed by controlled folding of the substrate to expose the interface between film and substrate for imaging. Figures 4(b–e) show the ZnO/PET interfaces. At 50 W, the interface appeared flat and continuous with no observable delamination or distortion. This uniformity was indicative of low residual stress and minimal thermal deformation at low deposition energies. However, as the power increased, notable changes in morphology have been

observed. At 100 W, the interface remained planar, although slight undulations began to emerge. These features were attributed to the moderate thermal expansion mismatch between the film and the substrate that caused localized stress accumulation. More interfacial distortion was observed at 150 W and 200 W, where the ZnO/PET interface showed a clear wavy structure. This morphological change was associated with thermal softening of PET during deposition. The increased ion bombardment and substrate heating at higher powers led to partial relaxation of the substrate. This deformation indicated a mechanical instability at the interface due to the difference in thermal expansion coefficients between two materials. This phenomenon induced a waviness of the substrate from the expanding film layer under compressive stress.

The crystalline quality of the ZnO films, including lattice parameter, stress, and crystalline grain size, was evaluated through XRD measurements. Figure 5(a) shows the 2θ–ω scans for all four samples. A vertical dashed line at 2θ = 34.4264° indicated the theoretical diffraction angle of the (002) plane of the ZnO wurtzite structure. The presence of a ZnO (002) peak in each sample confirmed film crystallinity. However, slight deviations in peak position relative to the ideal value suggested the existence of residual stress within films. Specifically, a shift of peak position to lower and higher 2θ indicated compressive and tensile stress, respectively. These peak shifts were a result of lattice distortion during growth. Variations in peak intensity and full width at half maximum (FWHM) were observed across the different samples. A reduction in peak intensity and an increase in FWHM correlated with degraded crystalline quality that was a result of increased defect density and reduced long-range order within the polycrystalline films.

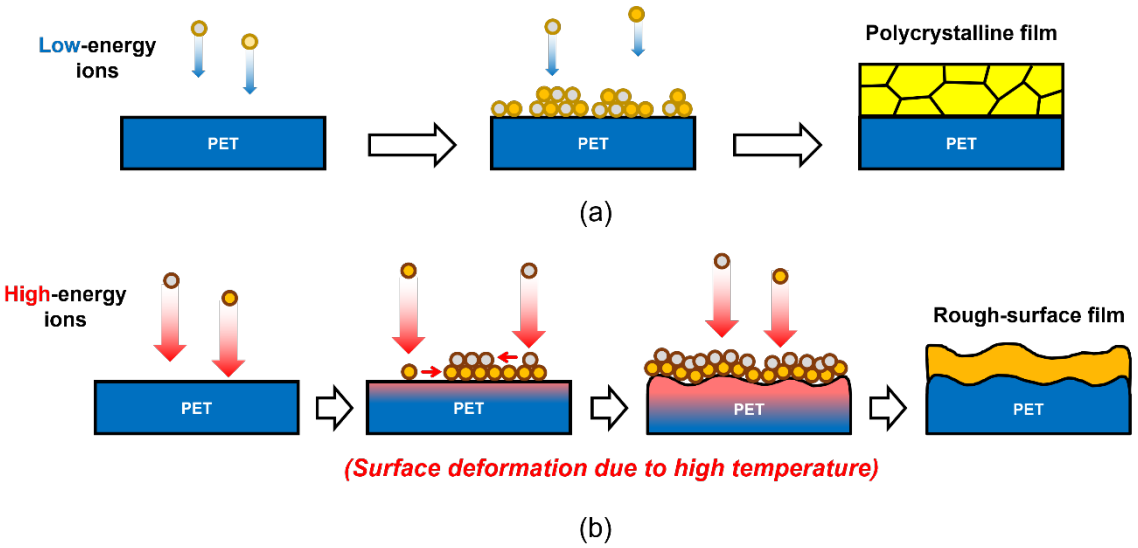

Figure 3. Schematic illustration of the deposition mechanisms during direct ZnO growth on PET substrates at (a) low, and (b) high RF power.

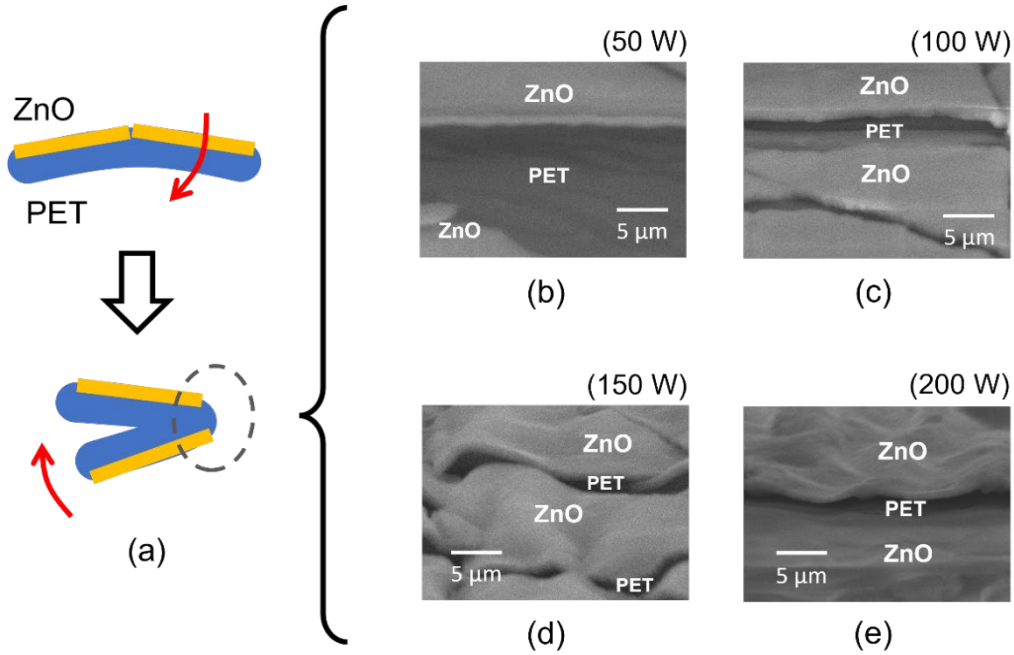

Figure 4. (a) Schematic of the sample preparation process for cross-sectional SEM imaging. (b–e) Cross-sectional SEM images of ZnO main films directly deposited on PET substrates at RF powers of (b) 50 W, (c) 100 W, (d) 150 W, and (e) 200 W.

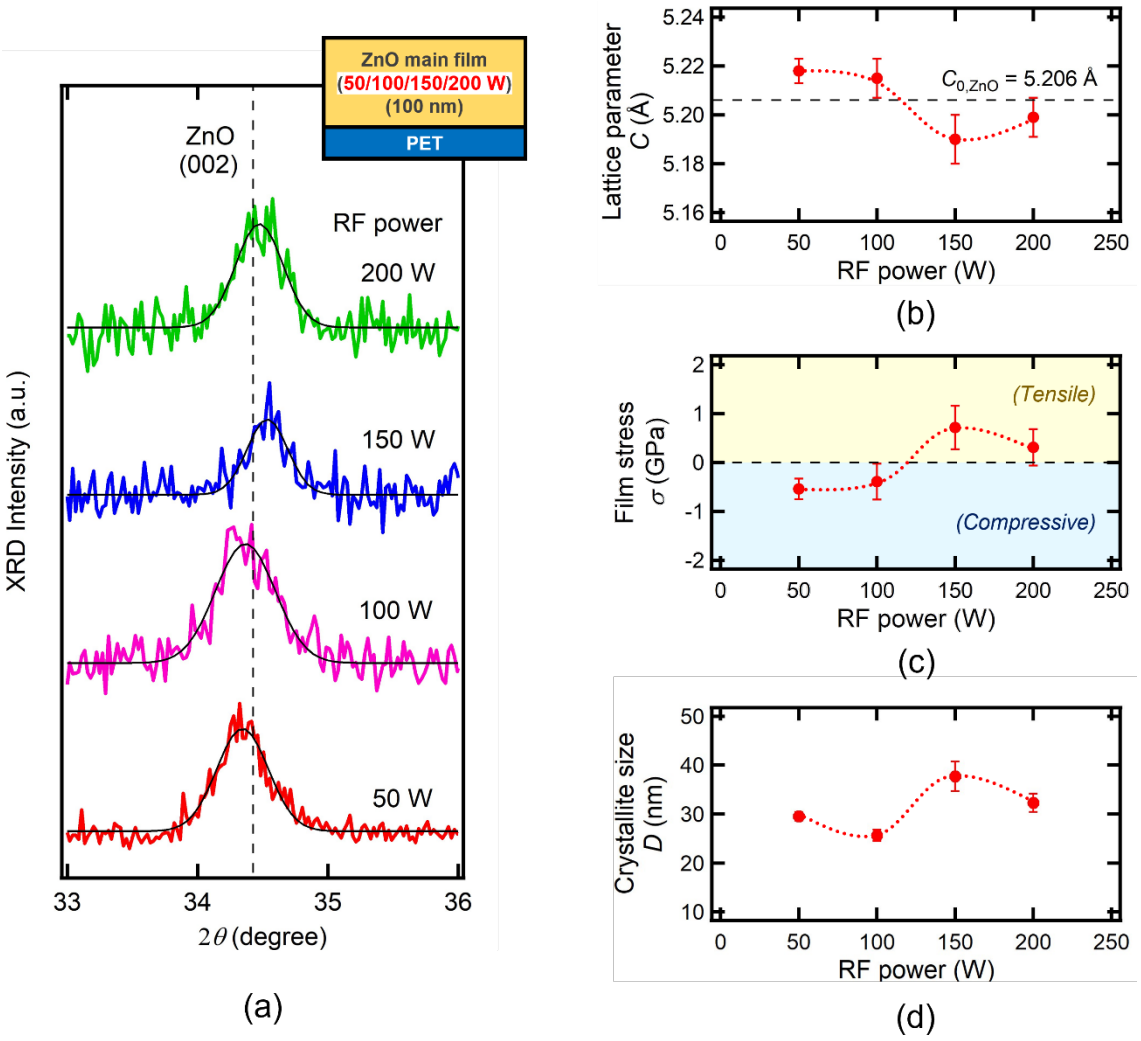

Figure 5. (a) 2θ–ω scans around the ZnO (002) plane. (b) Lattice parameter, (c) film stress, and (d) crystallite size extracted from the diffraction peaks and plotted as a function of applied RF power.

As shown in Figure 5(a), all diffraction peaks have been fit using the Gaussian distribution function to extract the (002)-plane-related peak position (2θ(002)) and the FWHM. The lattice parameter (C) is determined from the peak position angle using Bragg's diffraction condition.

$$2d_{(002)} \sin\theta_{(002)} = \lambda \tag{1}$$

where λ is the X-ray wavelength (= 1.5406 Å), and $d_{(002)}$ is the spacing between the (002) plane of ZnO. C could be determined from $2d_{(002)}$. The film stress (σ) is calculated using the formula [13,35].

$$\sigma = \frac{2c_{13}^2 - c_{33}(c_{11}+c_{12})}{2c_{13}}\left(\frac{C-C_0}{C_0}\right) \tag{2}$$

where c_{11}, c_{12}, c_{13} and c_{33} are the elastic constants (for ZnO, c_{11} = 208.8 GPa, c_{12} = 119.7 GPa, c_{13} = 104.2 GPa and c_{33} = 213.8 GPa), and C_0 is the unstrained lattice parameter of ZnO (= 5.206 Å). The crystallite size (D) is calculated using the Scherrer Equation.

$$D = \frac{k\lambda}{\beta\cos\theta_{(002)}} \tag{3}$$

where β is the FWHM of the diffraction peak, and k is a shape factor, typically set at 0.9.

Figure 5(b) shows the variation of C with RF power. As the power increased from 50 W to 100 W, C slightly decreased but remained above C_0 which has been marked by the horizontal dashed line. C decreased below C_0 at the power of 150 W, followed by a slight increase at 200 W. These deviations from C_0 indicated the occurrence of residual stress and possible point defects within the crystal. The non-monotonic trend in C suggested dynamic interplay during film growth, which was possibly stimulated by deposition-related thermal effects, lattice mismatch, and defect relaxation mechanisms.

Figure 5(c) shows the in-plane σ as a function of RF power. The stress transitioned from compressive to tensile with increasing power. At low power, the slightly negative value implied initial compressive stress, which was associated with limited atomic mobility and the early-stage coalescence of ZnO grains. As the power increased, the stress shifted to tensile. This tensile stress was due to enhanced adatom mobility and thermal expansion effects that dominated σ at higher deposition energies. At 200 W, a slight reduction in tensile stress suggested a partial relaxation or a redistribution of internal stress.

Despite these variations, all σ values remained relatively close to zero. This result indicated the ZnO films had low residual stress, which was advantageous for ensuring mechanical integrity on flexible PET substrates.

Figure 5(d) shows the dependency of D on RF power. At low powers (50 W and 100 W), D remained moderate around 25 nm to 30 nm. These values indicated limited crystallite growth under low-energy conditions. At 150 W, D increased substantially and reached approximately 40 nm. This result showed the improved crystalline quality that was facilitated by enhanced surface diffusion and atomic rearrangement. However, at 200 W, D slightly decreased, which resulted from increased defect incorporation or surface roughening at elevated powers. These XRD results suggested that the optimal power was about 150 W, where the film provided the largest crystallite size and improved crystallinity without significant stress accumulation.

Figure 6 shows the optical transmittance spectra of ZnO films directly deposited on PET substrates at different RF powers, plotted over the wavelength range of 300 nm to 650 nm. All samples provided sharp absorption edges at approximately 370 nm, corresponding to the intrinsic band gap of ZnO (~3.3 eV). The optical band gaps of the films could be estimated near this edge using the Tauc plot method [36]. At 50 W, the film demonstrated a relatively low transmittance of around 50% in the visible range. This limited optical transparency could be affected by the polycrystalline nature of the ZnO film, as shown by the AFM image in Figure 2(i). Although the film surface appeared smooth, the presence of numerous grain boundaries enhanced optical scattering, thereby reduced transmittance. Increasing the power to 100 W led to an improvement in optical transmittance reaching approximately 60%. This enhancement agreed with the evolution of film microstructure, as observed in the AFM image in Figure 2(j), where small crystallite grains disappeared and the crystal structure transitioned toward greater uniformity. This improved crystallinity resulted in fewer light-scattering sites and more efficient light transmission through the film. However, as the power increased above 100 W, the transmittance began to decline despite further improvements in crystalline quality, as confirmed by the XRD results. This decrease in transparency was caused by substrate deformation and the changes in surface morphology. Both SEM and AFM images showed that films grown at 150 and 200 W provided increasingly wavy surfaces and enhanced roughening. These surface irregularities behaved as a scattering center that significantly obstructed the passage of light and reduced the transmittance.

All above-mentioned results indicated the inherent limitations of directly depositing ZnO films onto PET substrates using RF magnetron sputtering. At low power, the films showed polycrystalline structures due to insufficient energy for proper atomic rearrangement. While increasing the power improved crystallinity and enhanced structural ordering, it also introduced significant thermal stress to the substrate. This stress was due to elevated substrate temperatures during deposition, which softened PET substrate and led to surface deformation as the temperature approached its glass transition or melting point [19,20]. As a result, the wavy surface unavoidably developed. These surface features degraded the film uniformity and its optical properties. This problem was particularly severe for the growth of thin ZnO layers where the film thickness was insufficient to mask the topographical distortions of the underlying substrate [21]. Thus, both the surface smoothness and thermal stability of the substrate were critical factors in achieving high-quality ZnO films, particularly when targeting thicknesses below 100 nm.

3.2 Two-step deposition: 100 nm ZnO/ZnO buffer/PET

The results from the direct deposition method demonstrated the sensitivity of surface quality to RF power. These underscored the need to optimize deposition parameters for achieving smoother thin films on flexible substrates. To solve these challenges, the two-step sputtering technique has been introduced. The growth mechanism and anticipated phenomena are illustrated in Figure 7. In this process, a buffer layer was first deposited onto the PET substrate, followed by the deposition of the main film in the second step. Both the main film and the buffer layer were produced under optimized conditions for the following reasons. For the main film, the power of 150 W was selected, as this condition had previously shown homogeneous and crack-free films with a maximum crystallite size. Although high power caused surface waviness and substrate deformation, these issues could be mitigated by the presence of the buffer layer. A power of 50 W was chosen for the buffer layer deposition since it yielded a layer with a smooth morphology. This layer mitigated thermal deformation by functioning as a heat-protective shield during the subsequent high-power deposition. Due to its higher thermal stability, the buffer layer not only maintained the structural stability of the substrate under elevated plasma conditions but also served as a structural template that promoted nucleation and epitaxial alignment of the main film. Given its dual role in providing thermal protection and enhancing nucleation, the buffer layer approach offered a practical method for optimizing buffer thickness to successfully integrate ZnO films into PET substrates.

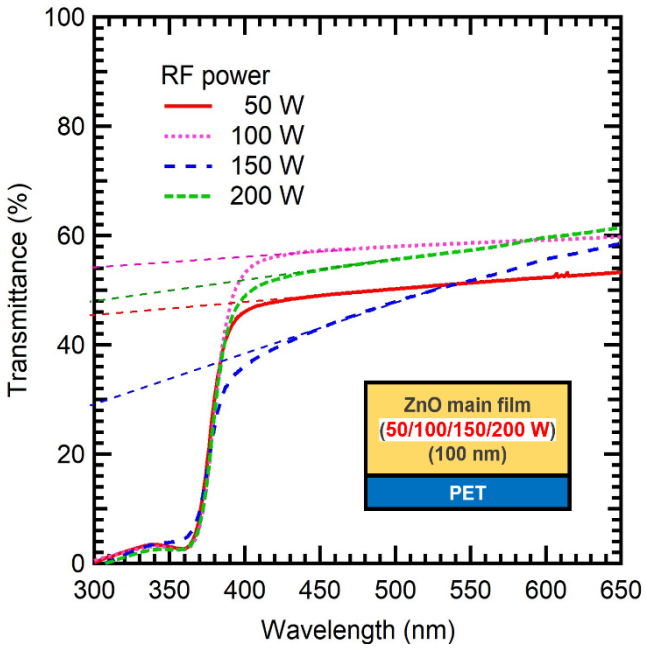

Figure 6. Optical transmittance spectra of ZnO main films directly deposited on PET substrates, measured over the wavelength range of 300 nm to 650 nm. Each spectrum corresponded to a sample deposited at different applied RF power.

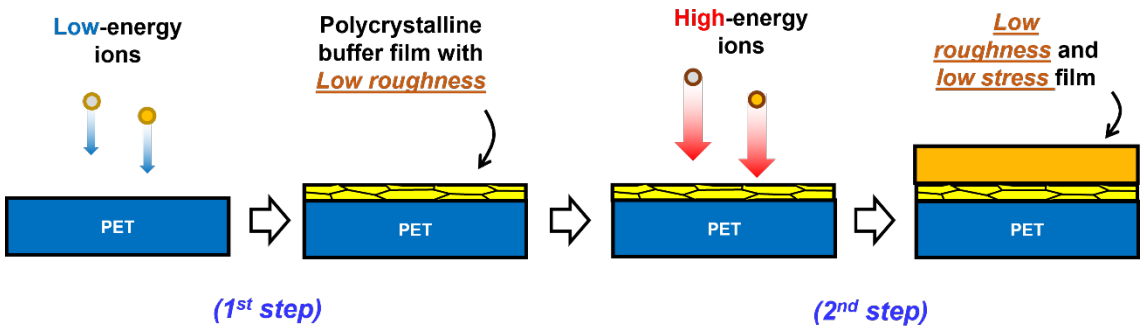

Figure 7. Schematic illustration of the deposition mechanisms during the two-step ZnO growth on PET substrates.

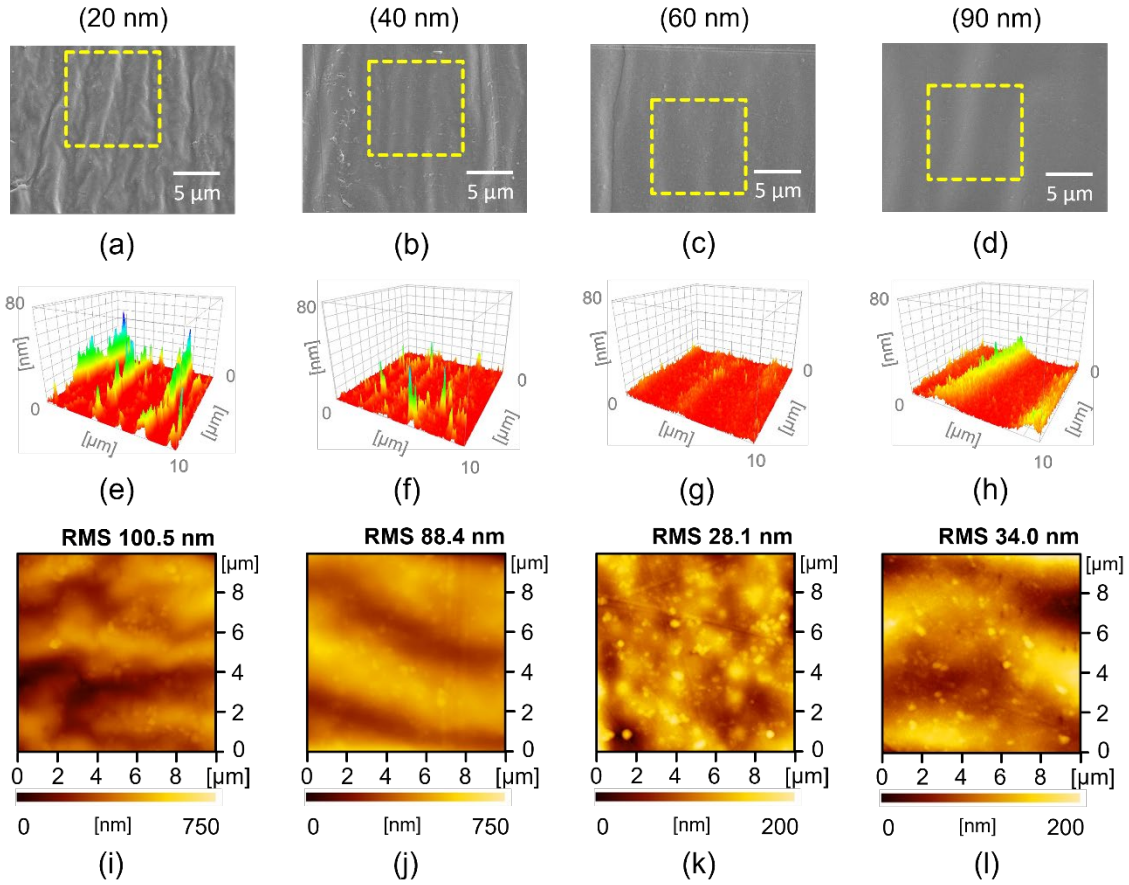

Figure 8. (a–d) SEM images, (e–h) 3D surface reconstructions from SEM data, and (i–l) AFM images showing the surface morphology of ZnO main films deposited on PET substrates with ZnO buffer layers of varying thicknesses from 20 to 90 nm.

The overall results for the 100 nm ZnO films on PET substrates, achieved using the two-step deposition technique with adjusted buffer layer thicknesses of 20 nm to 90 nm, were remarkably influenced by film qualities. Various buffer layer thicknesses yielded improved crystallinity and morphology, particularly roughness and stress. SEM images, illustrated in Figures 8(a–d), showed the clear trend that increasing the buffer layer thickness reduced surface irregularities and resulted in smoother surfaces with fewer ridges and valleys. When the buffer thickness reached above 60 nm, the surface became flatter and more uniform.

The 3D images, shown in Figures 8(e–h), reconstructed from the selected area of the original SEM images further illustrate the improvement in surface topography with increasing buffer thickness. These images provided spatial insight into the surface configuration and the height variation across each sample. The greatest surface deviation was observed in the 20 nm buffer sample, while a substantial reduction was observed in the 60 nm and 90 nm samples. These observations suggested that surface deformation caused by the underlying substrate had been suppressed. These supported the role of the buffer layer in improving surface morphology by reducing substrate-induced deformations.

The AFM images, shown in Figures 8(i–l), represented this improving trend in terms of RMS roughness. Each image covered an area of 10 µm × 10 µm. For buffer layer thicknesses of 20 nm, 40 nm, 60 nm, and 90 nm, the corresponding RMS values were 100.5 nm, 88.4, nm 28.1 nm, and 34.0 nm, respectively. The morphology

was enhanced compared to the film deposited directly at 150 W shown in Figure 2(k). The clear reduction at the 60 nm buffer thickness indicated a threshold above which further increases yielded only small improvement. This result suggested that a buffer thickness of 60 nm achieved an optimal balance, which was sufficient to planarize the surface and minimize excess material use.

Though previous studies used smaller AFM scan areas (2 μm × 2 μm), direct comparison of RMS values was not compatible with our scan area, which provided more representative surface uniformity over a device-relevant scale. Nevertheless, a consistent pattern of improvement could be observed with buffer-assisted growth. Previous works also reported corresponding improvement: Kim *et al.* [33] achieved the lowest RMS value using a 70 nm ZnO buffer. Lee *et al.* [32] significantly reduced RMS roughness with a 100 nm buffer. Park *et al.* [25] demonstrated significant enhancement with a 50 nm SiO_2 buffer.

The cross-sectional SEM images, shown in Figure 9, demonstrated the effect of buffer layer to reduced deformation and improved adhesion. The samples were prepared identically to those described in Figure 4(a). All the samples showed a consistently flat interface, compared to the sample deposited under the same power condition without a buffer layer, shown in Figure 4(d). This result indicated that the low-power-deposited ZnO buffer layer effectively suppressed substrate deformation during the subsequent high-power deposition of the ZnO main film. Since deformation of the flexible substrate typically led to increased surface roughness and morphological irregularities, this flatness of buffer layer was necessary for achieving a uniform main layer. When considered alongside the surface morphology, shown in Figure 8, the cross-sectional views further demonstrated the role of buffer layer as a structural stabilizer that facilitated the growth of high-quality ZnO main films. In contrast to single-step deposition, where high power alone compromised both the film and interface quality, the two-step deposition maintained smoother and more uniform film characteristics. Our results were consistent with previous reports [2,37], which also mentioned the importance of optimizing buffer layer thickness for a uniform ZnO film growth on flexible substrates without substrate-induced distortions.

These results were successfully achieved despite the use of a regular-grade PET, which had a significantly lower melting point than the epiready-grade substrates. By carefully optimizing the buffer layer thickness through the two-step process, this study demonstrated the feasibility of fabricating thin ZnO films with smooth surfaces on thermally sensitive PET substrates. This optimized two-step growth technique also proposed a practical pathway for cost-effective and scalable applications in flexible electronic devices.

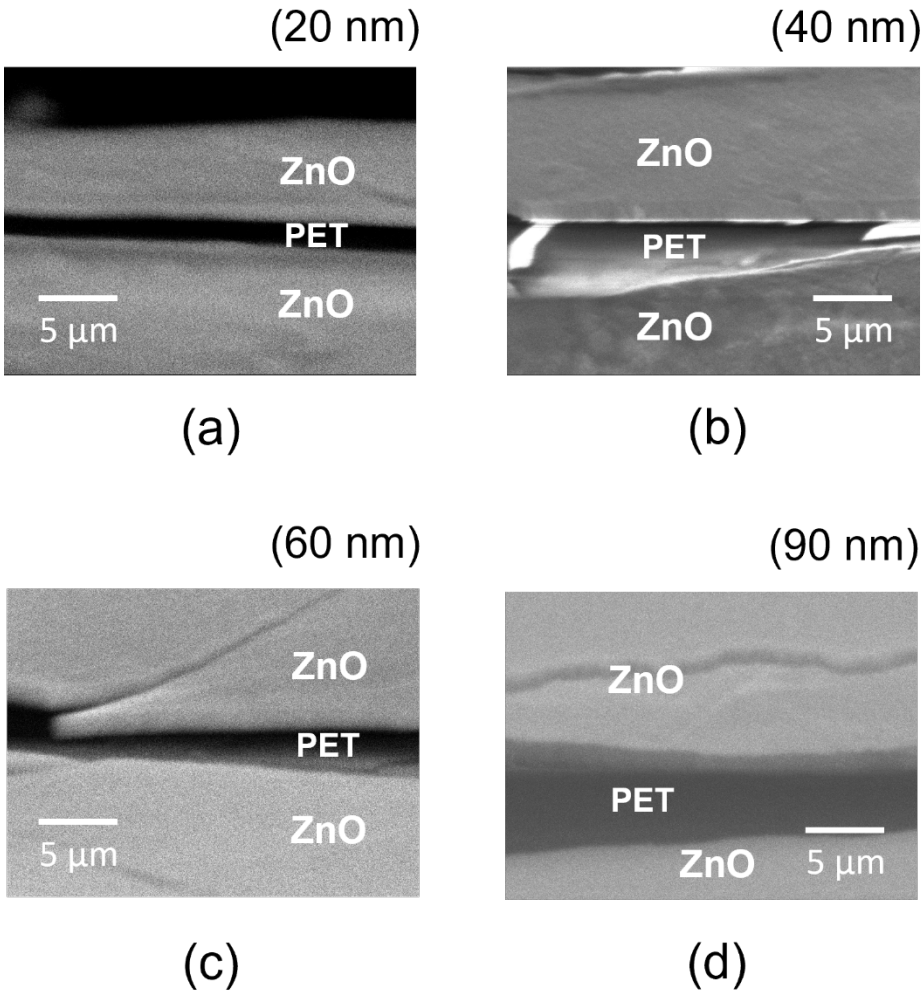

Figure 9. Cross-sectional SEM images of ZnO main films deposited on PET substrates with ZnO buffer layers of varying thicknesses: (a) 20 nm, (b) 40 nm, (c) 60 nm, and (d) 90 nm.

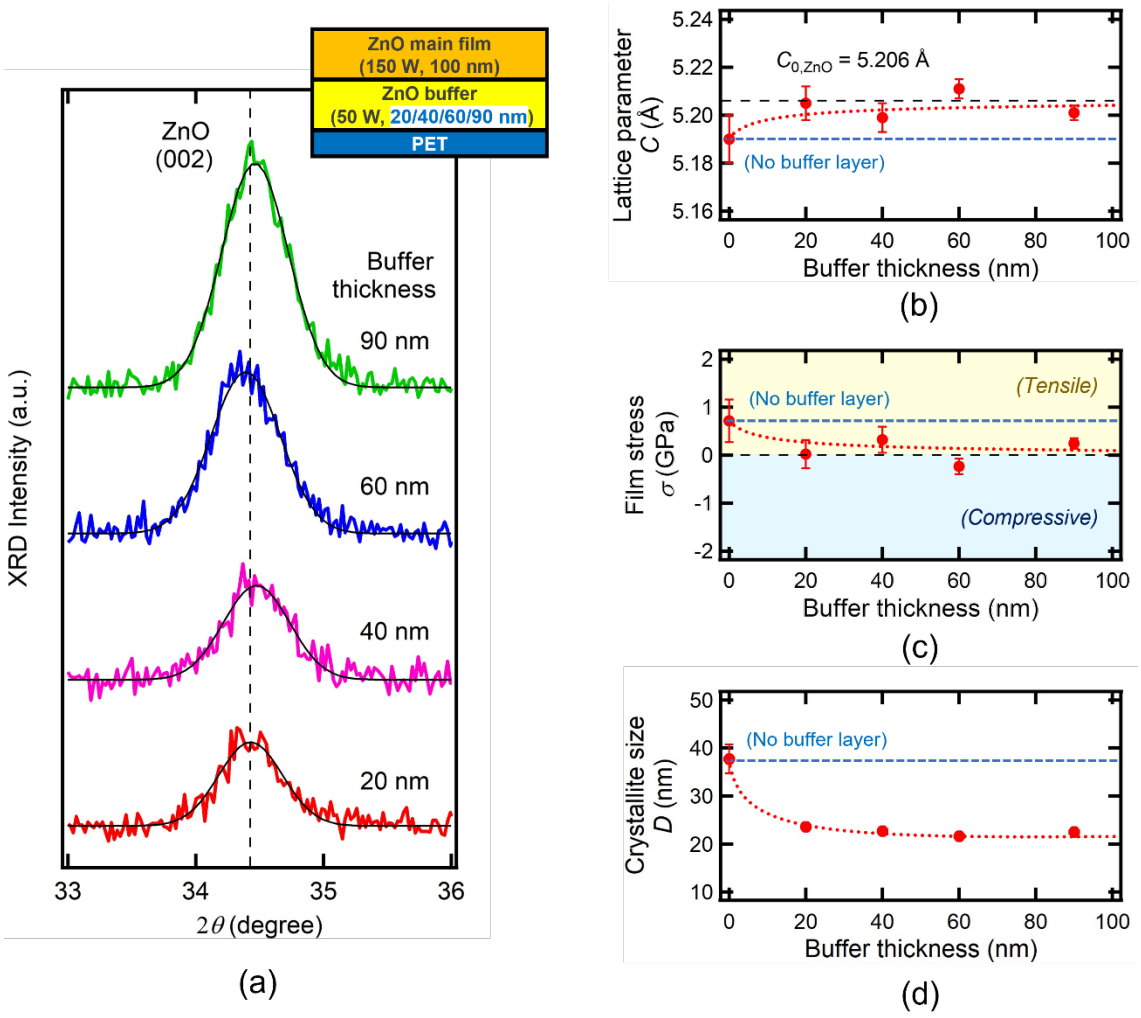

Figure 10. (a) 2θ–ω scans around the ZnO (002) plane. (b) Lattice parameter, (c) film stress, and (d) crystallite size extracted from the diffraction peaks and plotted as a function of ZnO buffer layer thickness.

The structural properties of the ZnO/ZnO buffer/PET samples with varying buffer layer thickness were further examined by XRD measurements. Figure 10(a) shows the results of 2θ–ω scans. A clear enhancement in the (002) diffraction peak intensity was observed with increasing buffer thickness. This result indicated improved c-axis orientation and overall crystallinity of the main film. This improvement contrasted with Figure 5(a), where the film deposited directly on PET without a buffer layer provided a lower diffraction peak intensity. This contrast supported the advantage of the buffer layer in improving crystal orientation and reducing defects in the main film.

Figures 10(b–c) show the evolution of structural quality through the changes in C and σ, respectively, as functions of buffer thickness. In the sample without a buffer layer, C significantly deviates from C_0. This result indicated lattice distortion induced by thermal mismatch and structural defects. In contrast, the buffered samples provided C much closer to C_0. The deviation of C significantly reduced and became nearly negligible at buffer thicknesses above 60 nm. This saturated value of C suggested the buffer layer behaved as a strain-relieving inter-layer, which absorbed mismatch-induced deformation. Consistently, the σ shows the inclusion of the buffer layer gradually reduced residual tensile stress in the main film. Without the buffer layer, the film contained substantial tensile stress, which not only degraded crystal quality but also affected increased surface roughness. As the buffer thickness increased, the stress transitioned toward more relaxed states to approach the stress-free region. This reduction in σ corresponded with improved crystal stability and reduced defect generation, both of which were essential for device-quality films.

Figure 10(d) shows a decrease in D with increasing buffer thickness. The value of D became saturated when the buffer thickness exceeded 60 nm. Compared to the unbuffered sample, which provided larger crystalline grains due to uninterrupted vertical growth, the buffered samples showed consistently smaller D. This result could be explained by the polycrystalline nature of the buffer layer, which introduced additional grain boundaries that hindered excessive grain coalescence in the upper main layer. Nevertheless, smaller D often suggested more grain boundaries. It could be advantageous in piezoelectric materials since fine crystallite could enhance mechanical stability, suppress dielectric loss, and maintain film quality during operation [11].

Our results aligned with the previous report. Rezaie *et al.* [38] described residual stress in thin films as a combination of intrinsic stress, arising from high-energy atomic bombardment and crystal defects, and extrinsic stress, related to mismatches in lattice constant and thermal expansion coefficient between the film and the substrate.

In the present study, the high power used in the single-step deposition without a buffer layer could stimulate both forms of residual stress. These stresses led to crystallographic distortion and rough surfaces. In contrast, the two-step deposition method incorporating a low-power buffer layer effectively separated the main film from the mechanical influence of the substrate. This technique could suppress stress accumulation and enhance morphological and structural uniformity.

Figure 11 shows the optical transmittance spectra of ZnO main film/ZnO buffer/PET samples measured across the 300 nm to 650 nm wavelength range. An absorption edge appeared near 370 nm, which was consistent with the intrinsic band gap of ZnO. The influence of buffer thickness on transmittance aligned with surface morphology trends observed in SEM and AFM images shown in Figure 8. The 20 nm buffer sample provided the lowest transmittance due to insufficient suppression of substrate-induced deformation and significant surface roughness. Increasing the thickness to 40 nm yielded only slight improvement. This observation suggested the buffer layer remained too thin to fully planarize the surface. The highest transmittance was observed at 60 nm, where surface flatness was optimal and light scattering was effectively minimized. Further increasing the buffer thickness to 90 nm resulted in a slight decrease in transmittance. This phenomenon was due to increased internal scattering or optical absorption within the thicker polycrystalline buffer layer. However, it was observed that the overall transmittance above the absorption edge remained relatively low (<30%), which was atypical for ZnO films. This reduction was primarily a result of light scattering caused by the polycrystalline nature of the ZnO buffer layer deposited at low power. Even though this deposition condition enhanced smooth surface formation, it compromised the crystalline quality of the buffer and increased optical scattering.

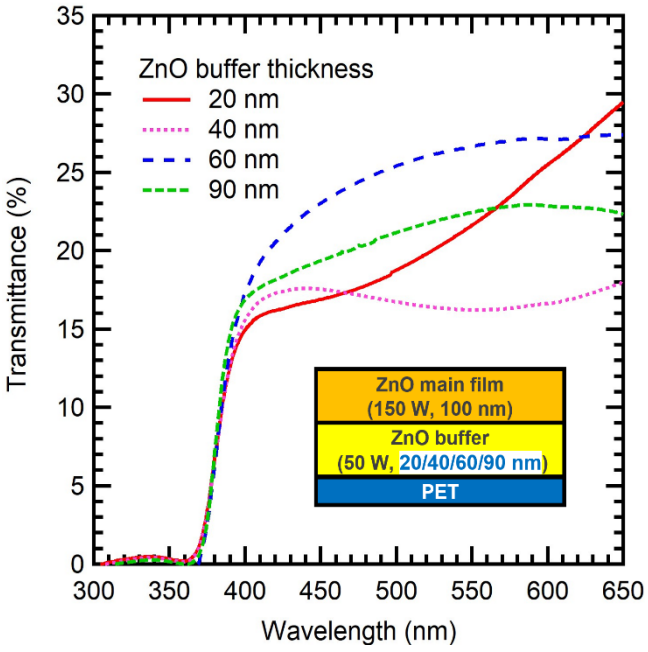

Figure 11. Optical transmittance spectra of ZnO main films deposited with ZnO buffer layers on PET substrates, measured over a wavelength range of 300 nm to 650 nm. Each spectrum corresponded to a sample with a different ZnO buffer layer thickness.

These results demonstrated that optical transmittance in ZnO films was not solely governed by surface smoothness, but also by an interplay of crystallinity, grain structure, and buffer thickness. Our observation highlighted that a 60 nm buffer layer offered an optimal balance between morphological smoothness and minimal light scattering, which was particularly important for optoelectronic applications. Moreover, achieving this performance using a regular-grade PET substrate further confirmed the practicality of the proposed two-step deposition method for low-cost, flexible optical devices.

4. Conclusions

This study demonstrated the challenges of fabricating high-quality, thin ZnO films on flexible, non-epiready PET substrates using direct RF magnetron sputtering at ambient temperature, where thermal sensitivity led to surface deformation, increased roughness, and limited crystalline quality. To overcome these limitations, the two-step deposition technique has been introduced using a low-power ZnO buffer layer, followed by high-power deposition of the main film. By optimizing the buffer thickness, particularly at 60 nm, the films exhibited significantly improved surface smoothness, reduced stress, stronger adhesion, and enhanced crystalline orientation. The stress-relieving function of the buffer layer assisted the lattice constant approach the ideal ZnO value, while the resulting fine grain size contributed to improved mechanical stability and reduced dielectric loss. These characteristics were beneficial for piezoelectric applications. Notably, these enhancements were achieved on commercially available PET substrates with lower thermal tolerance which underscored the practicality and cost-effectiveness of the proposed method for scalable integration of ZnO films in flexible electronic and sensor devices.\

Acknowledgements

This work was supported by the Thailand Graduate Institute of Science and Technology (TGIST) under Grant No. TGIST 01-57-047, the CU Graduate School Thesis Grant of Chulalongkorn University, and the Overseas Academic Presentation Scholarship for Graduate Students. The authors would also like to express their gratitude to the Nano Characterization Laboratory (NCL) at the National Nanotechnology Center (NANOTEC), Thailand, for their valuable support.

References

[1] N. Akin, Y. Ozen, H. I. Efkere, M. Cakmak, and S. Ozcelik, "Surface structure and photoluminescence properties of AZO thin films on polymer substrates," *Surface and Interface Analysis*, vol. 47, pp. 93–98, 2015.

[2] Y. Liu, X. Wang, Y. Han, and H. Chen, "Effect of deposition times of Al_2O_3 buffer layer on the structural and optical properties of AZO film on the polyethylene terephthalate substrates," *Bulletin of Materials Science*, vol. 41, pp. 106, 2018.

[3] D. Dimitrov, C.-L. Tsai, S. Petrov, V. Marinova, D. Petrova, B. Napoleonov, B. Blagoev, V. Strijkova, K. Y. Hsu, and S. H. Lin,

"Atomic layer-deposited Al-doped ZnO thin films for display applications," *Coatings*, vol. 10, no. 6, pp. 539, 2020.

[4] A. G. Martinez-Lopez, J. C. Tinoco, E. A. Elvira-Hernández, and A. L. Herrera-May, "Solution-processed ZnO energy harvester devices based on flexible substrates," *Microsystem Technologies*, vol. 29, pp. 205–210, 2023.

[5] S. Lee, K. Nam, W. Muhammad, D. Shin, S. Seo, and S.-D. Kim, "Influence of N_2O plasma treatment on PET-based flexible bending sensors with ZnO nanorod array cross-linked with interdigitated electrode structures," *Ceramics International*, vol. 48, pp. 25696–25704, 2022.

[6] H.-L. Shen, H. Zhang, L.-F. Lu, F. Jiang, and C. Yang, "Preparation and properties of AZO thin films on different substrates," *Progress in Natural Science: Materials International*, vol. 20, pp. 44–48, 2010.

[7] B. P. Nabar, Z. Celik-Butler, and D. P. Butler, "Self-powered tactile pressure sensors using ordered crystalline ZnO nanorods on flexible substrates toward robotic skin and garments," *IEEE Sensors Journal*, vol. 15, pp. 63–70, 2015.

[8] N. Promsawat, W. Wannasiri, P. Prawpraewa, C. Khwanruedee, P. Kantapon, P. Methee, and P. Janphuang, "A study of flexible piezoelectric generators by sputtering ZnO thin film on PET substrate," *Integrated Ferroelectrics*, vol. 195, pp. 220–229, 2019.

[9] P. Novák, "Possibilities of increasing the usability of sputtered AZO films as a transparent electrode," *Physica Status Solidi (a)*, vol. 216, pp. 1800814, 2019.

[10] H. S. Jo, C.-W. Park, S. An, A. Aldalbahi, M. El-Newehy, S. S. Park, A. L. Yarin, and S. S. Yoon, "Wearable multifunctional soft sensor and contactless 3D scanner using supersonically sprayed silver nanowires, carbon nanotubes, zinc oxide, and PEDOT:PSS," *NPG Asia Materials*, vol. 14, pp. 23, 2022.

[11] M. Wang, J. Wang, W. Chen, Y. Cui, and L. Wang, "Effect of preheating and annealing temperatures on quality characteristics of ZnO thin film prepared by sol–gel method," *Materials Chemistry and Physics*, vol. 97, pp. 219–225, 2006.

[12] W. W. Qin, Y. T. Li, T. Li, J. W. Qiu, X. J. Ma, D. Wei, X. Chen, X. F. Hu, and W. Zhang, "Microstructure-related piezoelectric properties of a ZnO film grown on a Si substrate," *Ceramics International*, vol. 42, pp. 16927–16934, 2016.

[13] S. Fernández, and F. B. Naranjo, "Optimization of aluminum-doped zinc oxide films deposited at low temperature by radio-frequency sputtering on flexible substrates for solar cell applications," *Solar Energy Materials and Solar Cells*, vol. 94, pp. 157–163, 2010.

[14] M.-C. Choi, Y. Kim, and C.-S. Ha, "Polymers for flexible displays: From material selection to device applications," *Progress in Polymer Science*, vol. 33, pp. 581–630, 2008.

[15] C. Lee, A. Park, Y. Cho, M. Park, W. I. Lee, and H. W. Kim, "Influence of ZnO buffer layer thickness on the electrical and optical properties of indium zinc oxide thin films deposited on PET substrates," *Ceramics International*, vol. 34, pp. 1093–1096, 2008.

[16] M. Hao, X. Lu, F. Sun, Y. Fu, Y. Ba, Y. Xie, and K. Liu, "Optoelectronic effect of Al-based buffer layers on Al-doped ZnO thin transparent conductive films on flexible substrates," *Optical Materials*, vol. 157, pp. 116179, 2024.

[17] A. N. Banerjee, C. K. Ghosh, K. K. Chattopadhyay, H. Minoura, A. K. Sarkar, A. Akiba, A. Kamiya, and T. Endo, "Low-temperature deposition of ZnO thin films on PET and glass substrates by DC-sputtering technique," *Thin Solid Films*, vol. 496, pp. 112–116, 2006.

[18] S. Ahmad, N. D. Md Sin, M. N. Berhan, and M. Rusop, "Effect of RF power on the structural properties of magnetron sputtered ZnO thin films deposited at room temperature," *Advanced Materials Research*, vol. 626, pp. 163–167, 2013.

[19] M. G. Faraj and K. Ibrahim, "Optical and structural properties of thermally evaporated zinc oxide thin films on polyethylene terephthalate substrates," *International Journal of Polymer Science*, vol. 2011, p. 302843, 2011.

[20] Z. Demircioğlu, E. Özkol, H. Nasser, and R. Turan, "Low temperature aluminum doped zinc oxide thin film deposition on ultra-thin flexible glass and PET substrates by RF magnetron sputtering," *Physica Status Solidi (c)*, vol. 12, pp. 1215–1219, 2015.

[21] K. Tang, S. Huang, S. Gu, S. Zhu, J. Ye, Z. Xu, and Y. Zheng, "The roles of buffer layer thickness on the properties of the ZnO epitaxial films," *Applied Surface Science*, vol. 388, pp. 557–564, 2016.

[22] R. Hong, J. Shao, H. He, and Z. Fan, "Influence of buffer layer thickness on the structure and optical properties of ZnO thin films," *Applied Surface Science*, vol. 252, pp. 2888–2893, 2006.

[23] A. Nahhas, H. K. Kim, and J. Blachere, "Epitaxial growth of ZnO films on Si substrates using an epitaxial GaN buffer," *Applied Physics Letters*, vol. 78, pp. 1511–1513, 2001.

[24] M. Wang, Y. Yang, P. Lan, K. Zhu, J. Huang, Y. Lu, R. Tan, and W. Song, "Ultra-thin (002)-oriented Al-doped zinc oxide transparent electrode grown on oxygen-controlled homo-seed layer," *Physica Status Solidi (RRL) – Rapid Research Letters*, vol. 8, pp. 172–175, 2014.

[25] J.-C. Park, S.-J. Kang, D.-H. Chang, and Y.-S. Yoon, "Properties of IZTO thin films deposited on PET substrates with the SiO_2 buffer layer," *Journal of the Korean Ceramic Society*, vol. 52, pp. 72–76, 2015.

[26] K. Koike, T. Komuro, K. Ogata, S. Sasa, M. Inoue, and M. Yano, "CaF_2 growth as a buffer layer of ZnO/Si heteroepitaxy," *Physica E: Low-dimensional Systems and Nanostructures*, vol. 21, pp. 679–683, 2004.

[27] A. Miyake, H. Kominami, H. Tatsuoka, H. Kuwabara, Y. Nakanishi, and Y. Hatanaka, "Luminescent properties of ZnO thin films grown epitaxially on Si substrate," *Journal of Crystal Growth*, vols. 214–215, pp. 294–298, 2000.

[28] N. Kumar, A. H. Chowdhury, B. Bahrami, M. R. Khan, Q. Qiao, and M. Kumar, "Origin of enhanced carrier mobility and electrical conductivity in seed-layer assisted sputtered grown Al doped ZnO thin films," *Thin Solid Films*, vol. 700, pp. 137916, 2020.

[29] W. Dong, X. Zhu, R. Tao, and X. Fang, "Effect of homo-buffer layers on the optical properties of ZnO thin films grown by pulsed laser deposition on Si (100)," *Journal of Materials Science: Materials in Electronics*, vol. 19, pp. 538–542, 2008.

[30] R. C. Chang, T. C. Li, and C. W. Lin, "Influence of various thickness metallic interlayers on opto-electric and mechanical

properties of AZO thin films on PET substrates," *Applied Surface Science*, vol. 258, pp. 3732–3737, 2012.

[31] F. Jia, Q. Wang, D. L. Zhu, S. Han, P. J. Cao, W. J. Liu, Y. X. Zeng, and Y. M. Lu, "Influence of ZnO buffer layers on the opto-electronic properties in Ga-doped ZnO thin films prepared by RF magnetron sputtering on PET substrates," *Journal of Materials Science: Materials in Electronics*, vol. 25, pp. 2934–2938, 2014.

[32] C. Lee, S. Kim, M. Park, S. Y. Park, W. I. Lee, and B. Lee, "Effects of a ZnO buffer layer on the resistivity and transmittance of GZO/AZO multilayer films deposited by R. F. magnetron sputtering on polymer substrates," *Transactions of the Materials Research Society of Japan*, vol. 32, pp. 911–915, 2007.

[33] S. Kim, W. Lee, and C. Lee, "Influence of ZnO buffer layer thickness on electrical and optical properties of GZO thin films deposited on polymer substrates," *Materials Science and Technology*, vol. 23, pp. 303–306, 2007.

[34] C. H. Tseng, C. H. Huang, H. C. Chang, D. Y. Chen, C. P. Chou, and C. Y. Hsu, "Structural and optoelectronic properties of Al-doped zinc oxide films deposited on flexible substrates by radio frequency magnetron sputtering," *Thin Solid Films*, vol. 519, pp. 7959–7965, 2011.

[35] Y. Zhang, Z. Fei, H. Huang, T. Lü, and R. Mu, "Influence of ZnO cap layer morphology on the electrical properties and thermal stability of Al-doped ZnO films," *Physica Status Solidi (a)*, vol. 217, p. 2000025, 2020.

[36] J. Tauc, R. Grigorovici, and A. Vancu, "Optical properties and electronic structure of amorphous germanium," *Physica Status Solidi (b)*, vol. 15, pp. 627–637, 1966.

[37] C.-Y. Tsay, and K.-C. Pai, "Properties of Al-Ga co-doped ZnO semiconductor thin films deposited on polyethylene terephthalate substrates by radio frequency magnetron sputtering," *Thin Solid Films*, vol. 654, pp. 11–15, 2018.

[38] M. N. Rezaie, N. Manavizadeh, E. Nadimi, and F. A. Boroumand, "Quality enhancement of AZO thin films at various thicknesses by introducing ITO buffer layer," *Journal of Materials Science: Materials in Electronics*, vol. 28, pp. 9328–9337, 2017.